Article:
Wu, F.-F., Zhou, D. orcid.org/0000-0001-7411-4658, Du, C. et al. (9 more authors) (2022) Design and fabrication of a C-band dielectric resonator antenna with novel temperature-stable Ce(Nb1–xVx)NbO4 (x = 0–0.4) microwave ceramics. ACS Applied Materials & Interfaces, 14 (43). pp. 48897-48906. ISSN 1944-8244

https://doi.org/10.1021/acsami.2c14627

Design and Fabrication of a C-band Dielectric Resonator Antenna with Novel Temperature Stable $Ce(Nb_{1-x}V_x)NbO_4$ (x = 0 - 0.4) Microwave Ceramics

Fang-Fang Wu,[1,5] Di Zhou,[1] Chao Du,[1] Diming Xu,*[1] Rui-Tao Li,[1] Ling Zhang,[1] Feng Qiao,[1] Zhong-Qi Shi,[2] Moustafa Adel Darwish,[3] Tao Zhou,[4] Heli Jantunen,[5] and Ian M. Reaney*[6]*

[1]Electronic Materials Research Laboratory, Key Laboratory of Multifunctional Materials and Structures, Ministry of Education, School of Electronic Science and Engineering, Xi'an Jiaotong University, Xi'an 710049, Shaanxi, China

[2]State Key Laboratory for Mechanical Behaviour of Materials, Xi'an Jiaotong University, Xi'an, 710049, P. R. China

[3]Physics Department, Faculty of Science, Tanta University, Al-Geish st., Tanta 31527, Egypt

[4]School of Electronic and Information Engineering, Hangzhou Dianzi University, Hangzhou, 310018, China

[5]Microelectronics Research Unit, P.O. Box 4500, FI-90014, University of Oulu, Finland

[6]Functional Materials and Devices Laboratory, Department of Materials Science and Engineering, University of Sheffield, S1 3JD, UK

*Corresponding Author: E-mail: zhoudi1220@gmail.com, diming.xu@xjtu.edu.cn, i.m.reaney@sheffield.ac.uk

Abstract: Vanadium (V)-substituted cerium niobate ($Ce(Nb_{1-x}V_x)O_4$: CNVx) ceramics were prepared to explore their structure-microwave property relations and application in C-band dielectric resonator antennas (DRAs). X-ray diffraction and Raman spectroscopy revealed CNVx ($0.0 \leq x \leq 0.4$) ceramics exhibited a ferroelastic phase transition at critical content of V ($x_c = 0.3$) from a monoclinic fergusonite to a tetragonal scheelite structure (T_{F-S}) which decreased in temperature as a function of x according to thermal expansion analysis. Optimum microwave dielectric performance was obtained for CNV0.3 with permittivity (ε_r) ~ 16.81, microwave quality factor (*Qf*) ~ 41,300 GHz (at ~8.7 GHz), and temperature coefficient of the resonant frequency, TCF ~ -3.5 ppm/°C. ε_r is dominated by Ce-O phonon absorption in the microwave band; *Qf* is mainly determined by porosity, grain size and the proximity of T_{F-S}, and TCF is controlled by the structural distortions associated with T_{F-S}. THz (0.20 - 2.00 THz, ε_r ~ 12.52 ± 0.70, tanδ ~ 0.39 ± 0.17) and infrared measurements are consistent, demonstrating that CNVx ($0.0 \leq x \leq 0.4$) ceramics are effective in the sub-millimeter as well as MW regime. A cylindrical DRA prototype antenna fabricated from CNV0.3 resonated at 7.02 GHz ($|S_{11}| = -28.8$ dB), matching simulations, with > 90% radiation efficiency and 3.34 - 5.93 dB gain.

Keywords: microwave dielectric ceramics, $CeNbO_4$, phase transition, thermally stable, C-band dielectric resonator antenna

Introduction

C-band (4 - 8 GHz) antennas are used in satellite communications, point to point wireless, search & track radars and fire control & imaging radars. Modern wireless

technology present new demands and challenges for antennas, necessitating high data transmission rates, high reliability and quality of transmission link to facilitate the development and improvement of Multiple-Input-Multiple-Output (MIMO) systems.[1-3] Dielectric Resonators Antennas (DRAs) are distinguished by their inherent advantages of low profile, low loss, high radiation efficiency, low metal loss, and omnidirectional response.[3-5] Microwave dielectric ceramics modulate antenna performance through optimization of 3 selective parameters: permittivity (ε_r), quality factor (*Qf*), and temperature coefficient of resonant frequency (TCF) which regulate the size and transmission speed, transmission loss and frequency selectivity and operating temperature stability, respectively.[6-8]

Rare earth niobate ($RENbO_4$, RE = La to Lu, Y) show promise for various applications due to their unique crystal chemistry.[9-11] $RENbO_4$ compounds undergo a ferroelastic phase transition (monoclinic fergusonite-type → tetragonal scheelite-type, T_{F-S}), accompanied by a distortion from [NbO_6] to [NbO_4] polyhedral coordination. The distortion is not only controlled by the RE ion radius (Bi^{3+} also substitutes on the A-site) but is also affected by the B-site ion radius of pentavalent substituents such as V, Sb and Ta, in a manner analogous to $BiVO_4$[8, 11-20], Figure 1. Most importantly, the structural distortion of the Nb-polyhedra associated with T_{F-S} is instrumental in controlling the dielectric properties of $RENbO_4$ compounds.[11] TCF may therefore be regulated by substitution of Nb with V ions in the $RENbO_4$ systems, approaching zero in the phase transition region, where T_{F-S} is close to room temperature. [11, 17, 21-22]

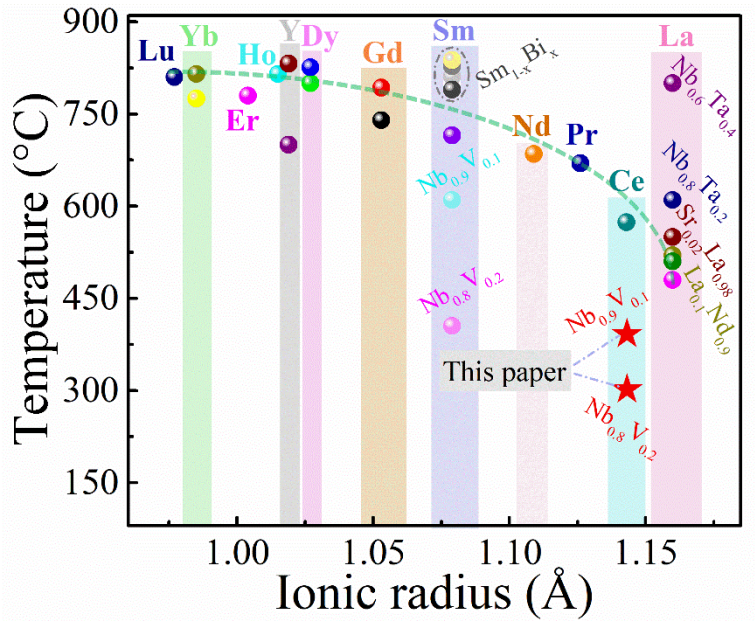

Figure 1 The onset temperature of the transition to the tetragonal scheelite phase in the rare-earth niobates as a function of the radius of the rare-earth ion.[8, 11, 13-14, 17, 19-20, 23-27]

Cerium niobite ($CeNbO_4$: CN) is an important member of the $RENbO_4$ family due its potential for use in solid oxide fuel cells (SOFCs)[24] and many studies report RE and V substitution on the Ce- and Nb-sites, respectively.[28-29] However, there are fewer studies which report their MW properties. Kim et al[11] presented data for most members of the $RENbO_4$ family but omitted $CeNbO_4$. Subsequently, Zhang et al[30] reported $CeNbO_4$ to have ε_r ~ 20.00 and Qf ~ 13,000 GHz at MW frequencies but did not mention TCF nor did they describe the underpinning mechanisms that control MW properties.

Our previous study revealed that the crystal structure and $T_{F\text{-}S}$ in the $RENbO_4$ (RE = La and Sm) system[17, 21] is controlled by the B-site substitution with V^{5+} ions, which optimize the microwave dielectric properties such that they are ideally suited for MW applications. The crystal structure, microstructures, thermal properties, and microwave dielectric properties of the $Ce(Nb_{1-x}V_x)O_4$ (CNVx) (x = 0 - 0.4) ceramics are therefore

investigated in this work with a view to optimizing their use in the design and fabrication of a C-band dielectric resonator antenna (DRA) for MIMO. The antenna is fabricated using CNV0.3 (ε_{DR} = 16.81), mounted on a Rogers RT5880 polymer board ($\varepsilon_{r,sub} = 2.20;\ tan\delta = 0.0009$)[2, 31-33] for potential use in point to point wireless (5.925 - 8.5 GHz)[34] and C-band radar applications.

Results and discussions

Figure 2 displays the XRD patterns and crystal structures of CNVx (x = 0 - 0.4) ceramics at optimum sintering temperature. At room temperature, compositions with 0 ≤ x ≤ 0.25 have the monoclinic fergusonite structure (12/c, JCPDS # 83-1912) but transform at critical content of V (x_c = 0.3) to a tetragonal scheelite structure (14_1/a, JCPDS # 79-2240), as evidenced by the merging of the diffraction peaks (-121) and (031) (Figure 2a), in agreement with Aldred et al.'s work.[35] V^{5+} substitution for Nb^{5+} generally stabilizes the high-temperature tetragonal scheelite phase of $RENbO_4$ at room temperature[35-36] as shown in Figure S1 (Supporting Information) with the extent of stabilization a function of the RE ion radius [17, 21, 35].

Rietveld refinements of CN and CNV0.3 are displayed in Figure 2(c, d) with crystallographic structural parameters provided in Table S1 and S2 (Supporting Information), respectively. The results for CNVx (x = 0.1, 0.2, and 0.25) are presented in Figure S2 (Supporting Information) and Table S1 and S2. As x increases, the monoclinic β angle decreases from 94.58º to 90º for x ≥ 0.3 (Figure 2b), where the tetragonal structure is stable at room temperature. Following standard crystallographic

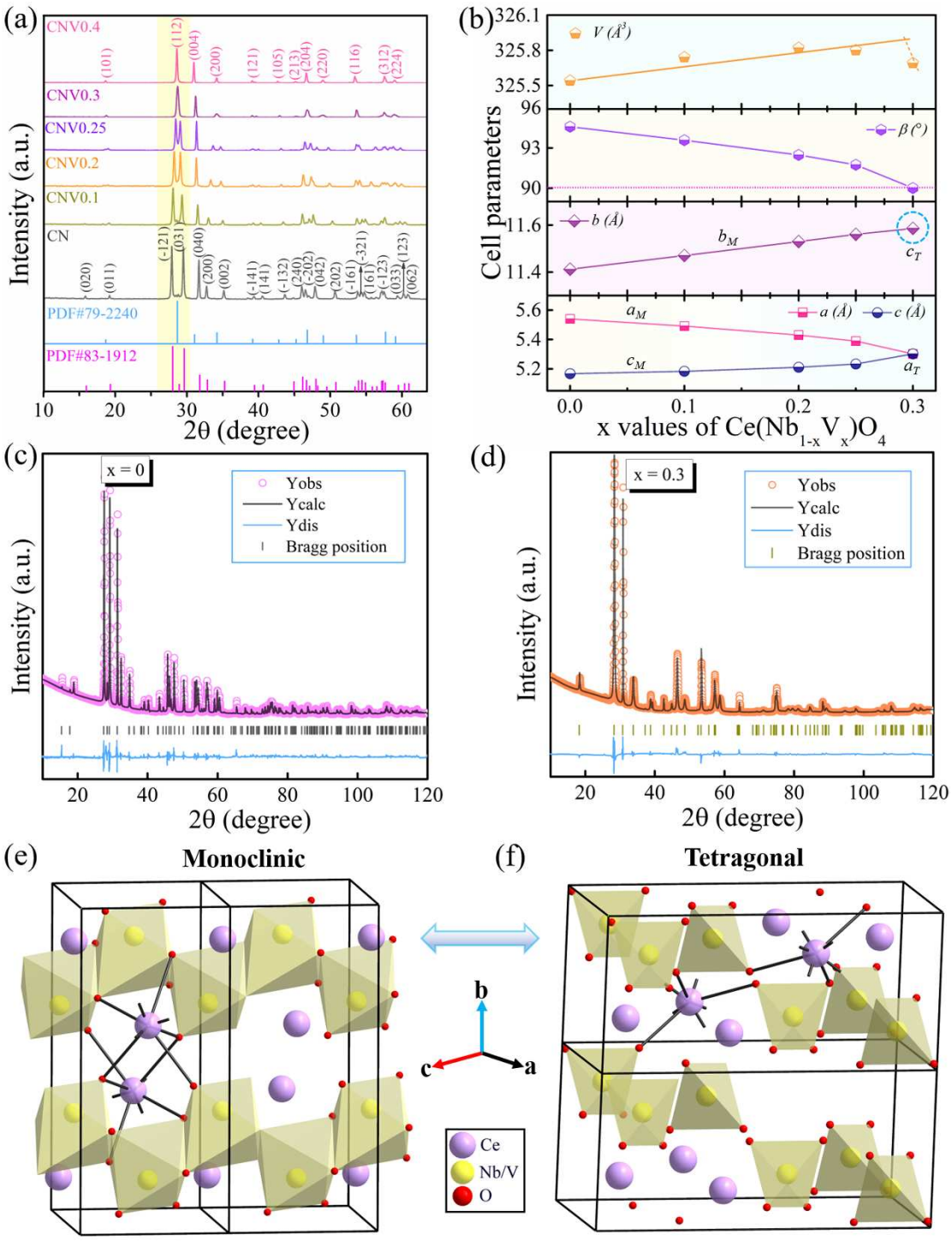

Figure 2 (a) X-ray diffraction patterns of the $Ce(Nb_{1-x}V_x)O_4$ (x = 0 - 0.4) ceramics. (b) Lattice constants as a function of x values. (c, d) Rietveld refinement plot of $Ce(Nb_{1-x}V_x)O_4$ (x = 0, 0.3) ceramics. (e, f) Schematic of crystal structure for $Ce(Nb_{1-x}V_x)O_4$ (x = 0, 0.3) ceramics.

conventions, the unit-cell dimensions a_m and c_m parameters of the monoclinic (m) cell become b_t and a_t in the tetragonal (t) structure with $b_m \equiv c_t$. Both c_m and b_m increased continuously before transformation to tetragonal, suggesting that the transition is

second order and accomplished through internal shear parallel to the z-axis as x increases[13]. The strain parameters, (e_1-e_2) and e_6 and the monoclinic angle β respectively, Figure S3 (Supporting Information), approach zero at the same value of x (x_c = 0.3). Surprisingly however, substitution of a smaller V^{5+} (r = 0.54 Å, CN = 6) for a larger Nb^{5+} (r = 0.64 Å, CN = 6)[12] ion leads to an increase rather than a decrease in the unit cell volume, principally due to the increase in the long axis ($b_m//c_t$).[35] The fergusonite lattice exhibits layers of edge-sharing octahedra [NbO_6], with the Ce ions, shown as spheres, dodecahedral in an eight-coordinate environment (Figure 2e). In contrast, the scheelite lattice consists of isolated [NbO_4] tetrahedra with the [SmO_8] units housed in chains of O ions shared with [NbO_4] (Figure 2f).

Evidence of the phase transition is also demonstrated by Raman spectroscopy in Figure S4 (Supporting Information). There are 18 ($8A_g + 10B_g$) (space group I2/a) and 15 Raman modes ($3A_g + 5B_g + 5E_g$) for the fergusonite scheelite structure (space group $I4_1/a$), respectively, predicted by Group theory.[37-40] The Raman modes of CNVx (x < 0.3) in fergusonite phase remain largely unchanged as a function of x, with only the A_g band at 801.3 and 321.5 cm^{-1} (stretching vibration of Nb-O bond), showing an increase in full width half maximum (FWHMs), attributed to the substitution of V^{5+} for Nb^{5+} which affects the rigidity of [NbO_6] polyhedra. The Raman spectra of CNVx (x ≥ 0.3) ceramics correspond well with those reported,[41] confirming a tetragonal scheelite structure, consistent with XRD data.

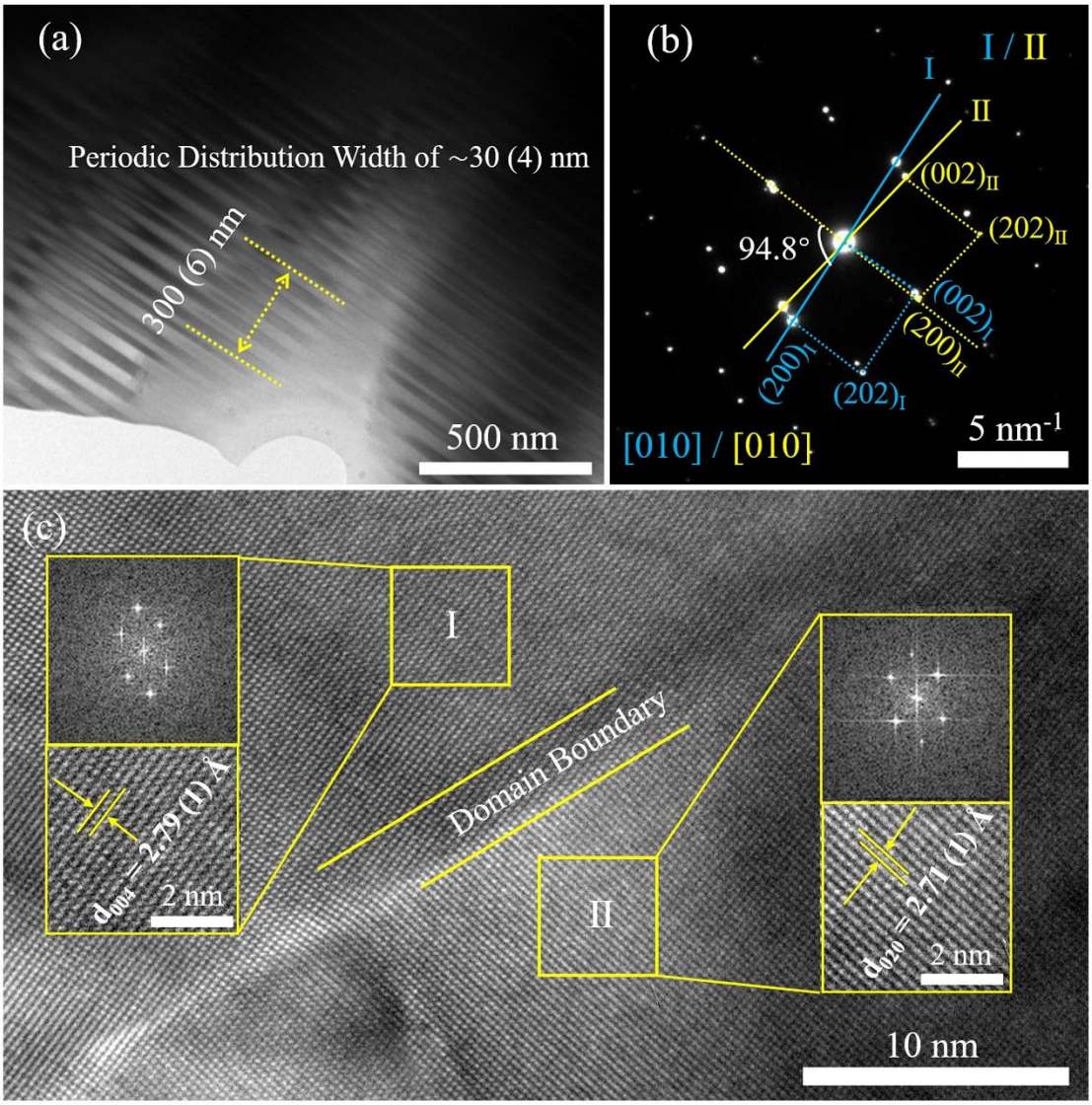

Figure 3. The HRTEM images of $CeNbO_4$ ceramic. (a) A section showing the parallel domains. (b) SAED patterns correspond to $CeNbO_4$ ceramic. (c) Magnified HRTEM image of the domain section.

Figure 3 shows room temperature TEM images of an undoped CN ceramic. Domains (30(4) nm) with a periodic distribution (Figure 3a) and lattice fringes (Figure 3c) are observed in the images, respectively. The domains arise due to the second-order ferroelastic phase transition from the scheelite (4/m) to fergusonite (2/m) structure. Alternate domains are described by different orientations (**I** and **II**) in the monoclinic fergusonite phase[8, 17, 42-46], as illustrated in the adjacent $[010]_m$ selected area electron diffraction pattern**,** Figure 3b. Each alternate domain has a 94.8° rotation, equivalent to the monoclinic β angle. The lattice fringes of the HRTEM images of the domains,

Figure 3c, were determined as 2.79(1) Å and 2.71(1) Å for zone **I** (004) and zone **II** (020) plane, respectively, consistent with XRD data.

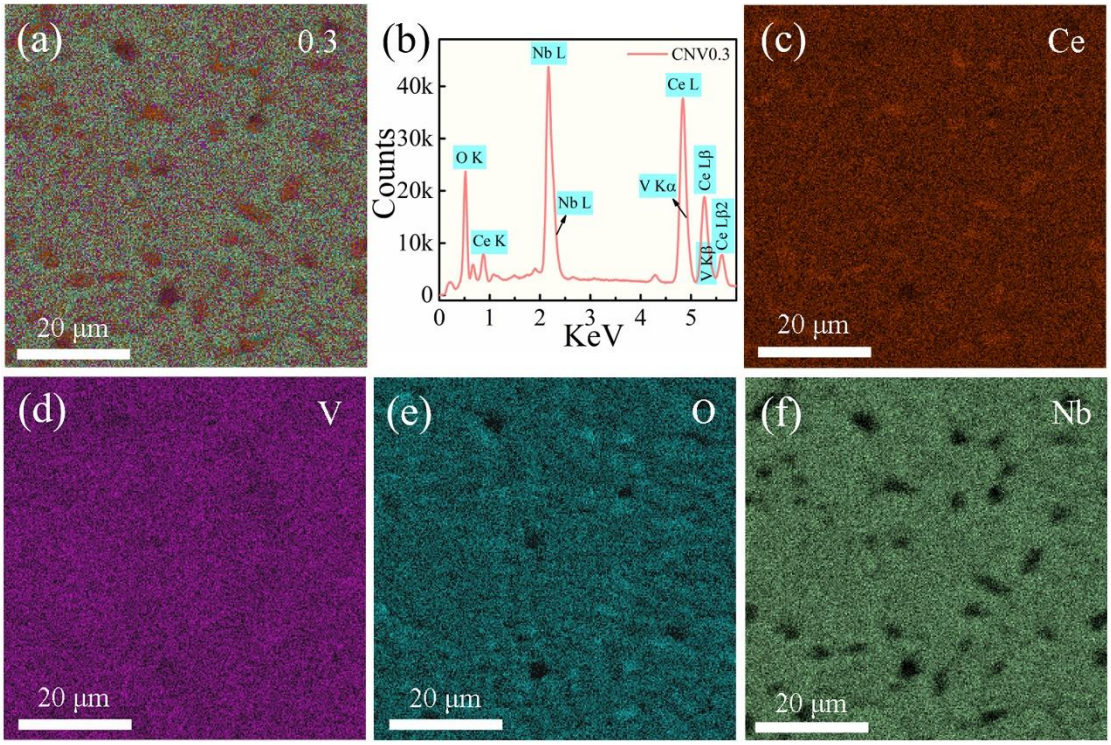

Figure 4 Sintered $Ce(Nb_{0.7}V_{0.3})O_4$ ceramic at optimal temperatures for (a) EDS elemental maps, (b) Spectra of EDS and (c-f) Elements are marked as their abbreviations.

SEM images of the polished surface microstructure of CNVx (x = 0 - 0.4) ceramics are shown in Figure S5 (Supporting information) which demonstrate a large grain size with some porosity. The mean grain size increased from 9.92 μm (CN) to 14.73 μm (CNV0.3) with increase in x, Figure S6 (Supporting information). Ce, Nb, V and O elements are uniformly distributed according to EDS analysis, Figure 4(a-f).

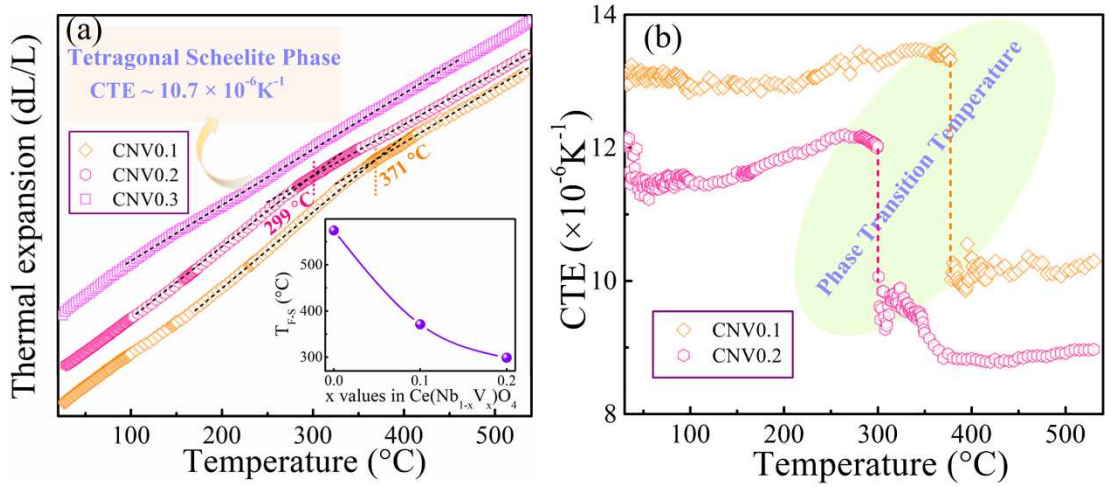

Figure 5 The thermal properties of $Ce(Nb_{1-x}V_x)O_4$ (x = 0.1, 0.2, and 0.3) ceramics: (a) deformation variation (phase transition temperatures vs. contents of V are shown in the inset), (b) coefficients of thermal expansion.

The phase transition of undoped CN from scheelite to fergusonite has been reported at 574 °C[24], at which temperature there is a discontinuity in the coefficient of thermal expansion (CTE). For CNV0.1 and CNV0.2, Figure 5a, the deformation varies linearly with temperature below and above T_{F-S}, and the T_{F-S} decreases as the V content increases (inset in Figure 5a), a phenomenon similar to the SNVx system.[17] The CTEs of CNV0.1 and CNV0.2 change abruptly at T_{F-S} (Figure 5b) and are larger in the fergusonite- (~ 11 - 13) than scheelite-type structures (~ 9 - 10). Rooksby reported that the distortion of $[NbO_4]$ tetrahedra determines the onset of T_{F-S}.[14] V^{5+} substitution decreases this distortion and thus the driving force for the fergusonite to scheelite transition reduces, along with T_{F-S}.

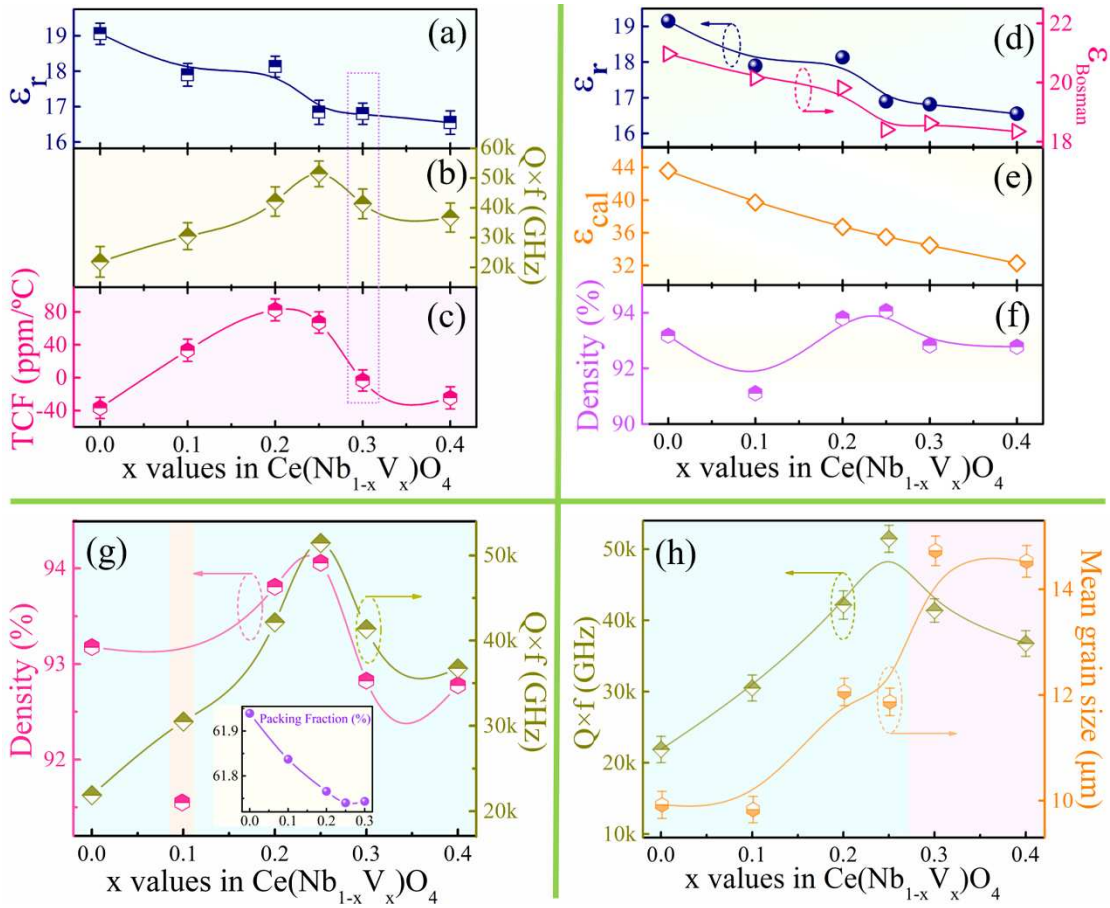

Figure 6 The properties of ε_r (a, d and e), $Q \times f$ (b, g and h), TCF (c), relative density (f, g), packing fraction (g), and mean grain size (h) of $Ce(Nb_{1-x}V_x)O_4$ ceramics as the functions of x.

The microwave dielectric properties and relative densities of optimized CNVx ceramics are displayed in Figure 6. We note that ε_r and *Qf* saturate in the sintering range, 1460-1500 °C, and then decrease marginally at higher temperatures. MW properties vs. sintering temperature are shown in Figure S7 (supporting information). For optimized composition, ε_r monotonously decreased from 19.15 to 16.55 as a function of x (Figure 6a, d), following a similar trend to the relative density (Figure 6f, g). Corrections for porosity using Bosman and Havinga's method[47-48] revealed that porosity has a limited effect on ε_r (Figure 6d). V^{5+} (2.92 $Å^3$) has a smaller ionic polarizability than Nb^{5+} (3.97 $Å^3$)[49] and thus its concentration, in principle, should be the dominant factor in ε_r. The measured ε_r and calculated ε_{cal} values are shown in

Figure 6(d, e) and follow the anticipated trend based on Shannon's additive rule and the Clausius-Mosotti relation, as in Eqs. (1) and (2).

$$a_x = a_{Ce^{3+}} + (1-x)a_{Nb^{5+}} + xa_{V^{5+}} + 4a_{o^{2-}} \quad (1)$$

$$\varepsilon_s = \frac{3Vm + 8\pi a_x}{3Vm - 4\pi a_x} \quad (2)$$

where α_{Ce}^{3+}, α_{Nb}^{5+}, α_{V}^{5+}, and α_{O}^{2-} are the polarizabilities of Ce^{3+}, Nb^{5+}, V^{5+}, and O^{2-}, respectively, and V_m is the molecular molar volume. The measured ε_r values (16.55 - 19.15) are smaller than ε_{cal} (32.27 - 43.57), possibly due to the complex distortions within the fergusonite structure[11] that suppress the polarizability of Nb^{5+} (effectively CN4 not CN6) and errors in the polarizabilities of lanthanides which may be lower than that reported by Shannon (Ce^{3+} = 6.15 Å^3), in comparison with Feteira (Ce^{3+} = 4.46 Å^3), whose values are taken from rare-earth aluminates[49-50]. Nonetheless, it can be concluded that as predicted ε_r is primarily modified through substitution of V^{5+} for Nb^{5+} in CNVx system. For compositions with $0.0 \leq x \leq 0.25$, *Qf* increased from 21,100 to 55,400 with an abrupt decrease at $x_c = 0.3$ (Figure 6b), consistent with the onset of the transition from fergusonite to scheelite[17, 21]. *Qf* is determined by a combination of intrinsic (fundamental interactions of the EM wave with the allowed phonon modes in the crystal structure) and extrinsic losses, such as porosity, point defects and grain boundaries. *Qf* increases with grain size for $0.0 \leq x \leq 0.25$ suggesting that extrinsic losses have been minimized (Figure 6h). The anomaly at $x_c = 0.3$ may relate only to the decrease in density for $x \geq 0.3$ but we also note that the packing fraction[51], Figure 6g, of the fergusonite and scheelite structures differ and *Qf* is inversely proportional to the packing fraction in the fergusonite region (inset of Figure 6g). This empirical

observation may be coincidental but requires further investigation. TCF increased with increasing x within the monoclinic-type region (Figure 6c), then abruptly decreased to become negative at x_c = 0.3, associated with the transition to the tetragonal scheelite structure.[21] TCF is a function of the temperature coefficient of ε_r (τ_ε) and the linear thermal expansion coefficient (a_L), as shown in Eq. (3):

$$TCF = -\left(\frac{\tau_\varepsilon}{2} + a_L\right) \qquad (3)$$

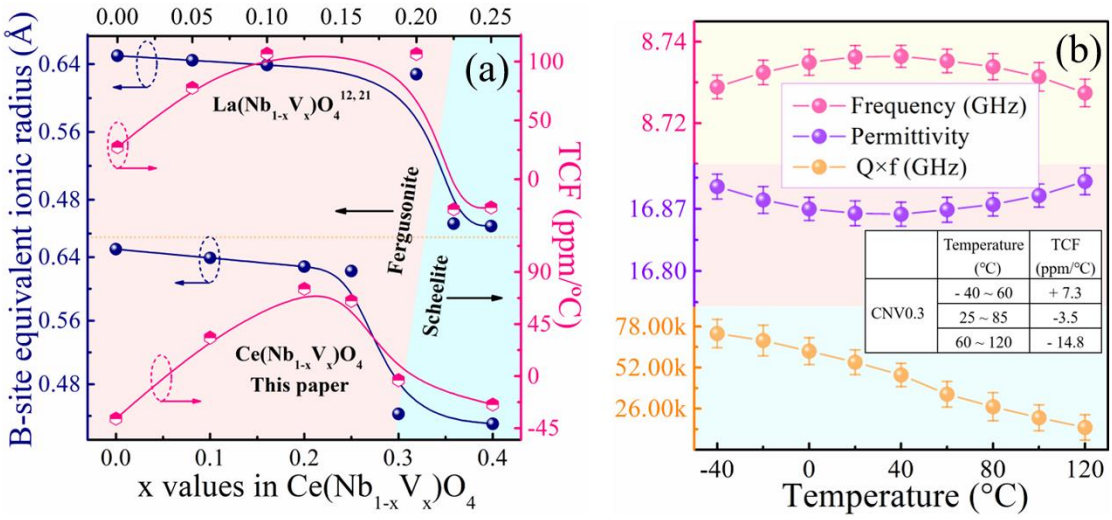

Figure 7 (a) The B-site equivalent ion radius and TCF of $RE(Nb_{1-x}V_x)O_4$ (RE = La, Ce) ceramics as the functions of x. (b) Variation of TCF for the $Ce(Nb_{0.7}V_{0.3})O_4$ ceramic as a function of temperature (from -40 to +120 °C).

a_L of CNVx ceramics varies from +11~13 and +9~10 ppm/°C for fergusonite and scheelite structure (Figure 5b), respectively, suggesting that the effect of a_L on the abrupt anomaly in TCF is limited which is mainly attributed to changes of τ_ε, dominated by the onset of $T_{F\text{-}S}$,[41] as shown in Figure 7a. To ensure the performance of MW devices at high temperature, the thermal stability of CNV0.3 ceramics was measured from -40 - +120 °C. As temperature increased, Figure 7b, the resonant frequency increased and then decreased, with ε_r exhibiting the opposite trend. *Qf* decreased with temperature but nonetheless was sufficiently high for the fabrication of

MW devices. The optimal microwave dielectric properties of the CNV0.3 ceramic is ε_r ~ 16.81, $Q \times f$ ~ 41, 300 GHz (at ~8.7 GHz), and TCF ~ -3.5 ppm/°C, ideal for the design and fabrication of MW devices.

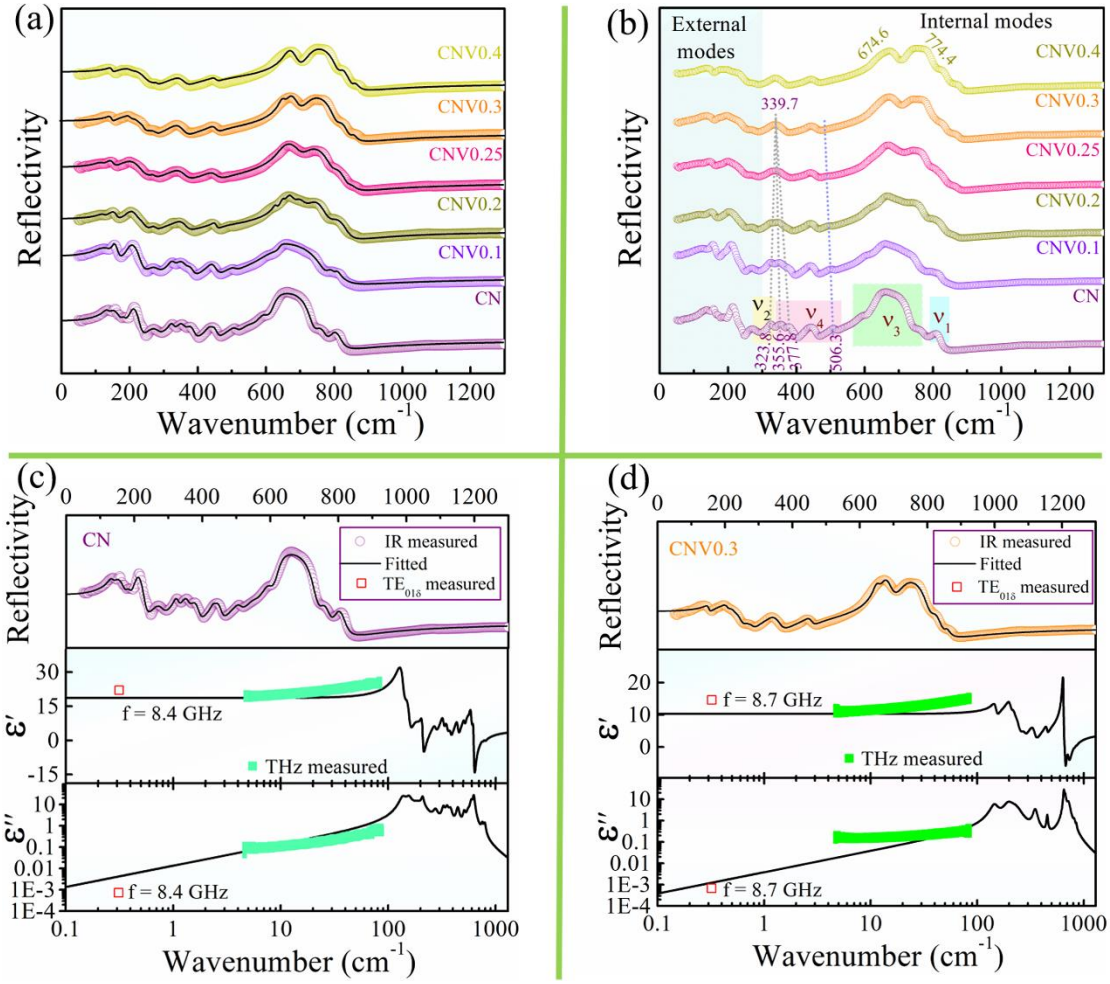

Figure 8 (a, b) Experimental and fitted infrared reflection spectra of $Ce(Nb_{1-x}V_x)O_4$ (x = 0 - 0.4) ceramics. (c, d) The complex dielectric spectrum of $CeNbO_4$ and $Ce(Nb_{0.7}V_{0.3})O_4$ ceramics (solid line −, circle ○ and square □ are fitted, experimental and measured values in microwave band. Square ■ is measured values in THz band; υ_1, υ_2, υ_3, and υ_4 corresponding to symmetric stretch, symmetric bending, antisymmetric stretch, and antisymmetric bending, respectively).

The measured and calculated infrared reflectance spectra of CNVx (x = 0 - 0.4) ceramics are displayed in Figure 8. Spectra are calculated according to Eqs. (4) and (5):

$$\varepsilon^*(\omega) - \varepsilon(\infty) = \sum_{j=1}^{n} \frac{\omega_{pj}^2}{\omega_{oj}^2 - \omega^2 - j\gamma_j\omega} \qquad (4)$$

$$R(\omega) = \left| \frac{1 - \sqrt{\varepsilon * (\omega)}}{1 + \sqrt{\varepsilon * (\omega)}} \right|^2 \quad (5)$$

The relevant parameters in Eqs. (4) and (5) were described in previous work.[8] All IR reflection spectra of CNVx ceramics in Figure 8a fit well using Eqs. (4) and (5). As x increases, some vibrational modes (Nb/V-O) below 400 cm^{-1} are merged as T_{F-S} is approached whereas the band at ~ 506.3 cm^{-1} progressively disappears. Figure 8(c, d) display the fitted complex dielectric spectrum of CN and CNV0.3 with the relevant phonon parameters shown in Table S3 (Supporting Information). ε_r of CN and CNV0.3 at optical frequencies are 4.38 and 3.78, and 18.54 and 10.24 at lower frequencies respectively, values close to those measured at MW frequencies, 19.15 at 8.4 GHz and 16.81 at 8.7 GHz, respectively, and indicating that ionic polarization dominates dielectric properties. External modes attributed to the Ce-O bond at < 300 cm^{-1} contribute most to ε_r indicating that the dielectric polarization depends on the phonon absorption of Ce-O bond in the microwave regime. Nb/V-O vibrational modes associated with the ferroelastic phase transition observed in the Raman and IR spectra give only a weak contribution to the microwave ε_r and their influence is neglected. The real part (ε′) of the permittivity obtained from the THz (0.2-2 THz) measurement agrees well with the experimental value as well as the IR, while the imaginary part (ε″) is still acceptable in the millimeter waves regime.

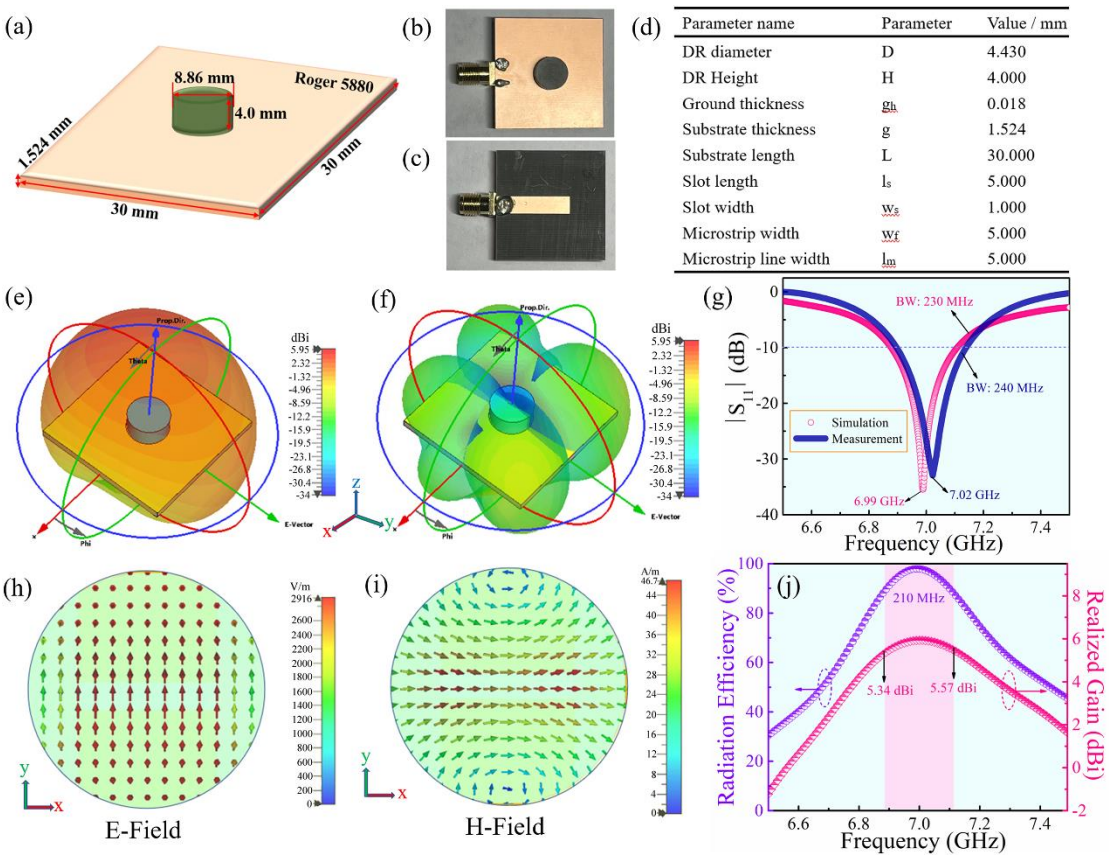

Parameter name	Parameter	Value / mm
DR diameter	D	4.430
DR Height	H	4.000
Ground thickness	g_h	0.018
Substrate thickness	g	1.524
Substrate length	L	30.000
Slot length	l_s	5.000
Slot width	w_s	1.000
Microstrip width	w_f	5.000
Microstrip line width	l_m	5.000

Figure 9 The geometries (unit: millimeter) of (a), top (b), bottom (c) views and design size (d) for the fabricated cylindrical dielectric resonator antenna (CDRA). The 3D simulated radiation patterns of co-polarized and cross-polarized (e-f) of the CDRA at the resonant frequency (6.99 GHz). The simulated and measured return loss $|S_{11}|$ of the proposed antenna (g). The simulation results of electric field (h) and magnetic field (i) at 6.99 GHz. Simulated antenna radiation efficiency and realized gain (j) of the CDRA.

A cylindrical DRA was fabricated using CNV0.3 ceramic as the dielectric resonator block/substrate (ε_{DR} = 16.82) mounted on a Rogers RT5880 polymer board ($\varepsilon_{r,sub} = 2.20;\ tan\delta = 0.0009$). Figures 9(a-d) show images of the design dimensions and prototype antenna. The 3D simulated radiation pattern of the DRA at the center frequency (6.99 GHz) of the C-band is shown in Figure 9(e, f). Figure 9g shows the measured and simulated return loss value ($|S_{11}|$) curves. The simulated $|S_{11}|$ of -35.45 dB at 6.99 GHz has return loss bandwidth of 230 MHz (6.88 - 7.11 GHz) compared with measured $|S_{11}|$ of -28.78 dB at 7.02 GHz with a return loss bandwidth of 240 MHz (6.91 - 7.15 GHz), confirming that CNVx ceramics are good candidates for commercial

satellite television transmission above 6 GHz in the C-band[2, 32-33], point to point wireless applications (5.925 - 8.5 GHz)[34], and C-band radar. The measured resonant frequency is displaced relative to the simulated value, potentially due to inaccurate placement of the DR, the presence of adhesive material, and connector mismatch.[1, 52-53] Figure 9(h, i) display the internal E- and H-fields of the $HE_{11\delta}$ mode at 6.99 GHz. The E-field is along the y-axis direction and H-field is a semi-circular magnetic field within the DRA (*xoy*-plane), indicating that the cylindrical CNV0.3 ceramic $HE_{11\delta}$ mode is activated. The simulated gain curve of the antenna and the radiation efficiency in the operating frequency range are shown in Figure 9j. The radiation efficiency of the designed antenna is > 90% from 6.89-7.20 GHz owing to the presence of a ceramic dielectric, with a corresponding gain range of 3.34 to 5.93 dB and 5.93 dB at the central resonant frequency (6.99 GHz).

Conclusions

The crystal structures of the CNVx (x = 0 - 0.4) ceramics were monoclinic fergusonite-type in the range of $x < 0.3$ and tetragonal scheelite-type for $x \geq 0.3$ according to XRD and Raman spectroscopy data. TEM revealed a ferroelastic domain structure formed on cooling from the high temperature scheelite to the low temperature fergusonite structure. ε_r at microwave frequencies is dominated by phonon absorption of the Ce-O vibrational modes. ε_r and *Qf* measured at 0.2 - 2 THz are consistent with the experimental MW as well as the infrared values, indicating that the ceramic is effective in the 5G and sub-millimeter wave regions. Control of TCF is achieved by tuning the structural distortion of the Nb polyhedra at $T_{F\text{-}S}$ through the substitution of

V^{5+} for Nb^{5+} with temperature stable compositions attained for $x_c = 0.3$ when the phase transition is close to room temperature. Optimal microwave dielectric properties were obtained for CNV0.3 ceramic with ε_r ~ 16.81, *Qf* ~ 41, 300 GHz (at ~8.7 GHz), and TCF ~ -3.5 ppm/°C. A cylindrical prototype DRA antenna with resonance at 7.02 GHz ($|S_{11}|$ = -28.78 dB) was designed and fabricated using CNV0.3 ceramic as the DR. Good agreement was observed between simulated and measured results with high radiation efficiency (> 90%) and gain (3.34 - 5.93 dB) achieved within the range of 6.89 - 7.10 GHz, which satisfies the working requirements of a C-band antenna.

Supporting Information

Experimental materials, methods, and characterization of CNVx (x = 0 - 0.4) ceramics; Dependence of the x_c of V^{5+} at phase transition on the ionic radius of the A- or B-site (Figure S1); Crystallographic structural parameters of CNVx (x = 0 - 0.3) ceramics (Table S1 and Table S2); Rietveld refinement plot of CNVx (x = 0.1, 0.2, 0.25) ceramics (Figure S2); Variation of strain and lattice parameters as a function of x (Figure S3); Raman spectra of CNVx (x = 0 - 0.4) ceramics (Figure S4); SEM images and mean grain size of the CNVx (x = 0 - 0.4) specimens (Figure S5 and Figure S6); microwave dielectric properties (ε_r and *Qf*) of CNVx (x = 0 - 0.4) ceramics as a function of temperature (Figure S7) and phonon parameters obtained by fitting the infrared reflection spectrum of CNVx (x = 0, 0.3) ceramics (Table S3).

Author contributions

D. Zhou and F. F. Wu: Carried out laboratory research, wrote the draft of the manuscript; C. Chao: Carried out design and performance measurement of antenna; D. M. Xu:

Carried out characterization of TEM; R. T. Li, L. Zhang and F. Qiao: Carry out characterization of dielectric performance; Z. Q. Shi, M. A. Darwish and T. Zhou: Carried out characterization of microstructural; H. Jantunen and I. M. Reaney reviewed the manuscript, improved the quality of English and corrected scientific inaccuracies and explanations.

Competing interests

The authors declare no competing financial interest.

Acknowledgements

This work was supported by the National Natural Science Foundation of China (51972260, 52072295), the International Cooperation Project of Shaanxi Province (2021KWZ-10), the Fundamental Research Funds for the Central University, the 111 Project of China (B14040). The authors thank the administrators in IR beamline workstation (BL01B) of National Synchrotron Radiation Laboratory (NSRL) for their help in the IR measurement and fitting. Scanning electron microscopy was carried out at the International Center for Dielectric Research (ICDR), Xi'an Jiaotong University, Xi'an, China. The authors thank Ms. Yan-Zhu Dai for the help in using SEM. The work on the project by Professor Reaney relates to Engineering and Physical Science Research Council Grants: EP/L017563/1 and EP/N010493/1.

References

(1) Kumari, T.; Das, G.; Sharma, A.; Gangwar, R. K. Design Approach for Dual Element Hybrid MIMO Antenna Arrangement for Wideband Applications. *International Journal of RF and Microwave Computer-Aided Engineering* **2019,** *29*, e21486.

(2) Kumar, J. P.; Karunakar, G. Compact C-Shaped MIMO Diversity Antenna for Quad Band Applications with Hexagonal Stub for Isolation Improvement. *International Journal of RF and Microwave Computer-Aided Engineering* **2019,** *30*, e22327.

(3) Anuar, S. U.; Jamaluddin, M. H.; Din, J.; Kamardin, K.; Dahri, M. H.; Idris, I. H. Triple Band MIMO Dielectric Resonator Antenna for LTE Applications. *International Journal of Electronics and Communications (AEÜ)* **2020,** *118*, 153172.

(4) Mishra, N. K.; Das, S.; Vishwakarma, D. K. Beam Steered Linear Array of Cylindrical Dielectric Resonator Antenna. *International Journal of Electronics and Communications (AEÜ)* **2019,** *98*, 106-113.

(5) Illahi, U.; Iqbal, J.; Sulaiman, M. I.; Alam, M.; Su'ud, M. M.; Khattak, M. I. Design and Development of a Singly-Fed Circularly Polarized Rectangular Dielectric Resonator Antenna for WiMAX/Satellite/5G NR Band Applications. *International Journal of Electronics and Communications (AEÜ)* **2020,** *126*, 153443.

(6) Guo, H. H. Z., D.; Du, C.; Wang, P. J.; Liu, W. F.; Pang, L. X.; Wang, Q. P,; Su, J. Z.; Singh, C.; Trukhanov, S. . Temperature Stable $Li_2Ti_{0.75}(Mg_{1/3}Nb_{2/3})_{0.25}O_3$-Based Microwave Dielectric Ceramics with Low Sintering Temperature and Ultra-low Dielectric Loss for Dielectric Resonator Antenna Applications. *Journal of Materials Chemistry C* **2020,** *8*, 4690-4700.

(7) Zou, Z. Y.; Lou, Y. H.; Song, X. Q.; Jiang, H.; Du, K.; Yin, C. Z.; Lu, W. Z.; Wang, X. C.; Wang, X. H.; Fu, M.; Lei, W. Near-Zero Thermal Expansion $Ba_{1-x}Sr_xZn_2Si_2O_7$-Based Microwave Dielectric Ceramics for 3D Printed Dielectric Resonator Antenna with Integrative Lens. *Advanced Materials Interfaces* **2021,** *8*, 2100584.

(8) Wu, F. F.; Zhou, D.; Du, C.; Jin, B. B.; Li, C.; Qi, Z. M.; Sun, S.; Zhou, T.; Li, Q.; Zhang, X. Q. Design of a Sub-6 GHz Dielectric Resonator Antenna with Novel Temperature-Stabilized $(Sm_{1-x}Bi_x)NbO_4$ (x = 0-0.15) Microwave Dielectric Ceramics. *ACS Applied Materials & Interfaces* **2022,** *14*, 7030-7038.

(9) Haugsrud, R.; Norby, T. Proton Conduction in Rare-Earth Ortho-Niobates and Ortho-Tantalates. *Nature Materials* **2006,** *5*, 193-196.

(10) Wang, X.; Li, X. P.; Cheng, L. H.; Xu, S.; Sun, J. S.; Zhang, J. S.; Zhang, X. Z.; Yang, X. T.; Chen, B. J. Concentration-Dependent Spectroscopic Properties and Temperature Sensing of $YNbO_4:Er^{3+}$ Phosphors. *RSC Advances* **2017,** *7*, 23751-23758.

(11) Kim, D. W.; Kwon, D. K.; Yoon, S. H.; Hong, K. S. Microwave Dielectric Properties of Rare-Earth Ortho-Niobates with Ferroelasticity. *Journal of the American Ceramic Society* **2006,** *89*, 3861-3864.

(12) Shannon, R. D. Revised Effective Ionic Radii and Systematic Studies of Interatomie Distances in Halides and Chaleogenides. *Acta Crystallographica* **1976,** *A32*, 751-767.

(13) Stubican, V. S. High-Temperature Transitions in Rare-Earth Niobates and TantaIates. *Journal of the American Ceramic Society* **1964,** *47*, 55-58.

(14) Rooksby, H. P.; White, E. A. D. The Structures of Compounds of Rare Earth Oxides with Niobia and Tantala. *Acta Crystallographica* **1963,** *16*, 888-890.

(15) Brixner, L. H.; Whitney, J. F.; Zumsteg, F. C.; Jones, G. A. Ferroelasticity in the $LnNbO_4$-type Rare Earth Niobates. *Materials Research Bulletin* **1977,** *12*, 17-24.

(16) Zhou, D.; Pang, L. X.; Guo, J.; Qi, Z. M.; Shao, T.; Yao, X.; Randall, C. A. Phase Evolution, Phase Transition, and Microwave Dielectric Properties of Scheelite Structured $xBi(Fe_{1/3}Mo_{2/3})O_4$-$(1-x)BiVO_4$ ($0.0 \leq x \leq 1.0$) Low Temperature Firing Ceramics. *Journal of Materials Chemistry* **2012,** *22*, 21412-21419.

(17) Wu, F. F.; Zhou, D.; Du, C.; Sun, S. K.; Pang, L. X.; Jin, B. B.; Qi, Z. M.; Varghese, J.; Li, Q.; Zhang, X. Q. Temperature Stable $Sm(Nb_{1-x}V_x)O_4$ ($0.0 \leq x \leq 0.9$) Microwave Dielectric Ceramics with Ultra-Low Dielectric Loss for Dielectric Resonator Antenna Applications. *Journal of Materials Chemistry C* **2021,** *9*, 9962-9971.

(18) Wachowski, S.; Mielewczyk-Gryn, A.; Gazda, M. Effect of Isovalent Substitution on Microstructure and Phase Transition of $LaNb_{1-x}MO_4$ (M=Sb, V or Ta; x=0.05-0.3). *Journal of Solid State Chemistry* **2014,** *219*, 201-209.

(19) Brandão, A. D.; Antunes, I.; Frade, J. R.; Torre, J.; Kharton, V. V.; Fagg, D. P. Enhanced Low-Temperature Proton Conduction in $Sr_{0.02}La_{0.98}NbO_{4-\delta}$ by Scheelite Phase Retention. *Chemistry of Materials* **2010,** *22*, 6673-6683.

(20) Vullum, F.; Nitsche, F.; Selbach, S. M.; Grande, T. Solid Solubility and Phase Transitions in the System $LaNb_{1-x}Ta_xO_4$. *Journal of Solid State Chemistry* **2008,** *181*, 2580-2585.

(21) Guo, D.; Zhou, D.; Li, W. B.; Pang, L. X.; Dai, Y. Z.; Qi, Z. M. Phase Evolution, Crystal Structure, and Microwave Dielectric Properties of Water-Insoluble (1-x)$LaNbO_4$-x$LaVO_4$ ($0 \leq x \leq 0.9$) Ceramics. *Inorganic chemistry* **2017,** *56*, 9321-9329.

(22) Solomon, S.; Kumar, M.; Surendran, K. P.; Sebastian, M. T.; Mohanan, P. Synthesis, characterization and properties of $[RE_{1-x}RE'_x]TiNbO_6$ dielectric ceramics. *Materials Chemistry and Physics* **2001,** *67*, 291-293.

(23) Jian, L.; Wayman, C. M. Monoclinic-to-Tetragonal Phase Transformation in a Ceramic Rare-Earth Orthoniobate, $LaNbO_4$. *Journal of the American Ceramic Society* **1997,** *80*, 803-806.

(24) Thompson, J. G.; Withers, R. L. Modulated Structures in Oxidized Cerium Niobates. *Journal of Solid State Chemistry* **1999,** *13*, 122-131.

(25) Sarin, P.; Hughes, R. W.; Lowry, D. R.; Apostolov, Z. D.; Kriven, W. M. High-Temperature Properties and Ferroelastic Phase Transitions in Rare-Earth Niobates ($LnNbO_4$). *Journal of the American Ceramic Society* **2014,** *97*, 3307-3319.

(26) Ramarao, S. D.; Murthy, V. R. K. Structural Phase Transformation and Microwave Dielectric Studies of $SmNb_{1-x}(Si_{1/2}Mo_{1/2})xO_4$ Compounds with Fergusonite Structure. *Physical Chemistry Chemical Physics* **2015,** *17*, 12623-12633.

(27) Zhang, P.; Feng, Y. J.; Li, Y.; Pan, W.; Zong, P. A.; Huang, M. Z.; Han, Y.; Yang, Z. S.; Chen, H.; Gong, Q. M.; Wan, C. L. Thermal and Mechanical Properties of Ferroelastic $RENbO_4$ (RE = Nd, Sm, Gd, Dy, Er, Yb) for Thermal Barrier Coatings. *Scripta Materialia* **2020,** *180*, 51-56.

(28) Packer, R. J.; Stuart, P. A.; Skinner, S. J. Structural Characterisation of the $Ce_{1-x}La_xNbO_{4+\delta}$ Solid Solution Series: In-situ High-Temperature Powder Diffraction Studies. *Journal of Solid State Chemistry* **2008,** *181*, 1445-1455.

(29) Packer, R. J.; Barlow, J.; Cott, A.; Skinner, S. J. Structure and Transport Properties of Vanadium Substituted Cerium Niobate. *Solid State Ionics* **2008,** *179*, 1094-1100.

(30) Zhang, Z. L.; Xu, C.; Liu, Q. P. Microwave Dielectric Properties of $RENbO_4$ (RE=Y, Yb,Ce) Ceramics. *Key Engineering Materials* **2010,** *434-435*, 217-220.

(31) Modak, S.; Khan, T.; Laskar, R. H. Penta-notched UWB Monopole Antenna Using EBG Structures and Fork-Shaped Slots. *Radio Science* **2020,** *55*, 11.

(32) Khan, M. I.; Chandra, A.; Das, S. Triple Band Dual Polarized Planar Slot Antenna. *2018 3rd International Conference on Microwave and Photonics (ICMAP 2018)* **2018**, 9-11.

(33) Alharbi, A. G.; Kulkarni, J.; Desai, A.; Sim, C. Y. D.; Poddar, A. A Multi-Slot Two-Antenna MIMO with High Isolation for Sub-6 GHz 5G/IEEE802.11ac/ax/C-Band/X-Band Wireless and Satellite Applications. *Electronics* **2022,** *11*, 473.

(34) Sharma, N.; Bhatia, S. S. Performance Enhancement of Nested Hexagonal Ring-Shaped Compact Multiband Integrated Wideband Fractal Antennas for Wireless Applications. *International Journal of RF and Microwave Computer-Aided Engineering* **2019,** *30*, 22079.

(35) Alared, A. T. Composition Dependence of Lattice Parameters Systems in $ANb_{1-x}V_xO_4$ Systems Where A = Ce, Nd*. *Journal of Solid State Chemistry* **1985,** *59*, 95-102.

(36) Aldred, A. T. Unusual Cell Volume Behavior in the $LaNb_{1-x}V_xO_4$ System. *Materials Letters* **1983,** *1*, 197-199.

(37) Tsunekawa, S.; Takei, H. Study on the Room Temperature Phase of $LaNbO_4$ Crystals. *Materials Research Bulletin* **1977,** *12*, 1087-1094.

(38) Hou, J.; Chen, Q.; Gao, C.; Dai, R.; Zhang, J.; Wang, Z.; Zhang, Z.; Ding, Z. Raman and Luminescence Studies on Phase Transition of $EuNbO_4$ under High Pressure. *Journal of Rare Earths* **2014,** *32*, 787-791.

(39) Nicol, M.; Durana, J. F. Vibrational Raman Spectra of $CaMoO_4$ and $CaWO_4$ at High Pressures. *The Journal of Chemical Physics* **1971,** *54*, 1436-1440.

(40) Christofilos, D.; Kourouklis, G. A.; Ves, S. A High Pressure Raman Study of Calcium Molybdate. *Journal of Physics and Chemistry of Solids* **1995,** *56*, 1125-1129.

(41) Zhou, D.; Guo, H. H.; Fu, M. S.; Yao, X. G.; Lin, H. X.; Liu, W. F.; Pang, L. X.; Singh, C.; Trukhanov, S.; Trukhanov, A.; Reaney, I. M. Anomalous Dielectric Behaviour during the Monoclinic to Tetragonal Phase Transition in $La(Nb_{0.9}V_{0.1})O_4$. *Inorganic Chemistry Frontiers* **2021,** *8*, 156-163.

(42) Li, J.; Huang, C. M.; Xu, G. B.; Wayman, C. M. The Domain Structure of $LaNbO_4$ in the Low Temperature Monoclinic Phase. *Materials Letters* **1994,** *21*, 105-110.

(43) Li, J.; Wayman, C. M. Domain Boundary and Domain Switching in a Ceramic Rare-Earth Orthoniobate $LaNbO_4$. *Journal of the American Ceramic Society* **1996,** *79*, 1642-1648.

(44) Tsunekawa, S.; Kasuya, A.; Nishina, Y. Shape and Size Controls of Micro-Domains in $LaNbO_4$ Crystals. *Materials Science & Engineering* **1996,** *A217/218*, 215-217.

(45) Zhang, Z. L.; Zhou, L.; Hu, Y. G.; Jiang, L. Preparation and Characterization of Al_2O_3-$LaNbO_4$ Composites. *Scripta Materialia* **2002,** *47*, 637-641.

(46) Ma, B.; Chi, B.; Pu, J.; Li, J. In Situ TEM Observation of Domain Switch in $LaNbO_4$ Added to NiO-Y_2O_3 Stabilized ZrO_2 Ceramic Composite. *Scripta Materialia* **2014,** *92*, 55-58.

(47) Bosman, A. J.; Havinga, E. E. Temperature Dependence of Dielectric Constants of Cubic Ionic Compounds. *Physical Review* **1963,** *129*, 1593-1600.

(48) Zhou, D.; Pang, L. X.; Yao, X.; Wang, H. Influence of Sintering Process on the Microwave Dielectric Properties of $Bi(V_{0.008}Nb_{0.992})O_4$ Ceramics. *Materials Chemistry and Physics* **2009,** *115*, 126-131.

(49) Shannon, R. D. Dielectric Polarizabilities of Ions in Oxides and Fluorides. *Journal of Applied Physics* **1993,** *73*, 348-366.

(50) Feteira, A.; Sinclair, D. C.; Lanagan, M. T. Structural and Electrical Characterization of $CeAlO_3$ Ceramics. *Journal of Applied Physics* **2007,** *101*, 064110.

(51) Kim, E. S.; Chun, B. S.; Freer, R.; Cernik, R. J. Effects of Packing Fraction and Bond Valence on Microwave Dielectric Properties of $A^{2+}B^{6+}O_4$ (A^{2+}: Ca, Pb, Ba; B^{6+}: Mo, W) Ceramics. *Journal of the European Ceramic Society* **2010,** *30*, 1731-1736.

(52) Roshni, S. B.; Arun, S.; Sebastian, M. T.; Mohanan, P.; Surendran, K. P. Low κ Mg_2SiO_4 Ceramic Tapes and Their Role as Screen Printed Microstrip Patch Antenna Substrates. *Materials Science and Engineering: B* **2021,** *264*, 114947.

(53) Xiang, H. C.; Kilpijärvi, J.; Myllymäki, S.; Yang, H. T.; Fang, L.; Jantunen, H. Spinel-Olivine Microwave Dielectric Ceramics with Low Sintering Temperature and High Quality Factor for 5 GHz Wi-Fi Antennas. *Applied Materials Today* **2020,** *21*, 100826.

ToC Figure:

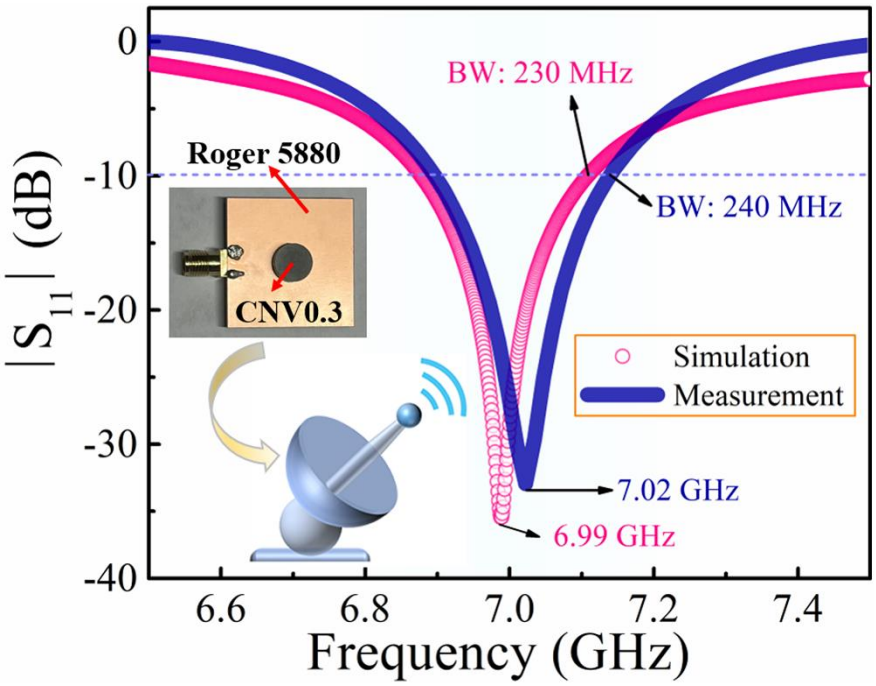
0
-10
-20
-30
-40
|S11| (dB)
6.6
6.8
7.0
7.2
7.4
Frequency (GHz)
BW: 230 MHz
BW: 240 MHz
Roger 5880
CNV0.3
Simulation
Measurement
7.02 GHz
6.99 GHz